

Generalized bilinear Koopman realization from input-output data for multi-step prediction with metaheuristic optimization of lifting function and its application to real-world industrial system

Shuichi Yahagi, *Membership*, Ansei Yonezawa, *Membership*, Heisei Yonezawa, *Membership*, Hiroki Seto, *Membership*, and Itsuro Kajiwara

arXiv:2602.15422v1 [eess.SY] 17 Feb 2026

Abstract—This paper introduces an input-output bilinear Koopman realization with an optimization algorithm of lifting functions. For nonlinear systems with inputs, Koopman-based modeling is effective because the Koopman operator enables a high-dimensional linear representation of nonlinear dynamics. However, traditional approaches face significant challenges in industrial applications. Measuring all system states is often impractical due to constraints on sensor installation. Moreover, the predictive performance of a Koopman model strongly depends on the choice of lifting functions, and their design typically requires substantial manual effort. In addition, although a linear time-invariant (LTI) Koopman model is the most commonly used model structure in the Koopman framework, such model exhibit limited predictive accuracy. To address these limitations, we propose an input-output bilinear Koopman modeling in which the design parameters of radial basis function (RBF)-based lifting functions are optimized using a global metaheuristic algorithm to improve long-term prediction performance. Consideration of the long-term prediction performance enhances the reliability of the resulting model. The proposed methodology is validated in simulations and experimental tests, with the airpath control system of a diesel engine as the plant to be modeled. This plant represents a challenging industrial application because it exhibits strong nonlinearities and coupled multi-input multi-output (MIMO) dynamics. These results demonstrate that the proposed input-output bilinear Koopman model significantly outperforms traditional linear Koopman models in predictive accuracy.

Index Terms—Bilinear system, Data-driven modeling, Koopman operator, Nonlinear system, Diesel engine, Industrial application

Manuscript received Month xx, 2xxx; revised Month xx, xxxx; accepted Month x, xxxx. This work was supported in part by the ISUZU Advanced Engineering Center, Ltd.

Shuichi Yahagi (*Corresponding author*) is with Department of Mechanical Engineering, Tokyo City University, 1-28-1 Tamazutsumi, Setagaya-ku, Tokyo 158-8557, Japan (e-mail: yahagisi@tcu.ac.jp).

Ansei Yonezawa is with Department of Mechanical Engineering, Kyushu University, 744 Motoooka, Nishi-ku, Fukuoka 819-0395, Japan.

Heisei Yonezawa and Itsuro Kajiwara are with Division of Mechanical and Aerospace Engineering, Hokkaido University, N13, W8, Kita-ku, Sapporo, Hokkaido 060-8628, Japan.

Hiroki Seto are with 6th Research Department, ISUZU Advanced Engineering Center Ltd., 8 Tsutidana, Fujisawa-shi, Kanagawa 252-0881, Japan.

I. INTRODUCTION

A. Motivation

System identification is essential for enabling system prediction, control, and fault detection. Traditional system identification methods, such as Auto-Regressive with eXogenous (ARX) models and Numerical Algorithms for Subspace State Space System Identification (N4SID) [1] have proven highly effective for linear systems. However, identifying models for highly nonlinear industrial systems remains challenging, which in turn complicates the control of complex industrial processes. To address this issue, data-driven approaches for nonlinear systems have been proposed, including the Koopman operator framework [2], [3], [4], deep learning methods such as recurrent neural networks (NNs) and long short-term memory (LSTM) networks [5], nonlinear ARX (NARX) models [6], and sparse identification of nonlinear dynamics (SINDY) [7], [8].

The Koopman operator is formulated as a linear operator in an infinite-dimensional space by mapping the original state space to a higher-dimensional space through lifting functions [9], [10]. Its ability to represent a nonlinear system as a linear model is a distinctive feature not found in other data-driven approaches. Although Koopman operator theory inherently deals with infinite-dimensional spaces, in practical computations, a finite-dimensional approximation of the Koopman operator can be identified from data using dynamic mode decomposition (DMD) [11], [12] and extended DMD (EDMD) [13], [14]. The resulting Koopman model can accurately capture the original nonlinear behavior by leveraging a high-dimensional linear structure. This enables the application of conventional linear control theory [2], [15], [16]. Despite these achievements, several challenges for application to industrial systems remain, including the selection of lifting functions that significantly impact prediction performance, the inherent limitations of linear model predictions, and the unavailability of measurements for the full system states.

B. Related work

It has been noted that LTI Koopman models may not adequately capture the control-affine dynamics of nonlinear systems, which makes accurate prediction challenging [17].

To address this limitation, bilinear Koopman realizations have been investigated. These models offer improved predictive accuracy compared to LTI Koopman models while remaining computationally more efficient than fully nonlinear Koopman approaches [18]. Theoretical foundations of bilinear Koopman realizations have been explored in [18], [19]. In addition, methods for computing bilinear lifting functions using deep NNs have been proposed [20], [21], [22]. The choice of the observation function that maps state variables to observable variables—commonly referred to as the lifting function—has a significant impact on the predictive performance of the Koopman model. According to [23], previous approaches for designing lifting functions include mechanics-inspired selections, empirical selections such as monomials and polynomials, and RBF functions with randomly assigned centers. Another proposed approach employs highly contributory basis functions derived from SINDy modeling [24], [25]. However, these methods often fail to ensure reproducibility or improve the predictive accuracy of model identification. To address these limitations, recent research has explored neural network-based approaches for lifting function design [26], [27]. Nevertheless, NN-based methods present challenges such as hyperparameter tuning, overfitting, model complexity, computational cost, and issues related to vanishing or exploding gradients. Furthermore, the orthogonality of NN-based lifting functions is not guaranteed. To date, meta-heuristic approaches such as particle swarm optimization (PSO) have not been investigated for lifting function design.

Previously, LTI and bilinear Koopman realizations typically assumed that all system states and inputs were measurable. However, in practical industrial applications, it is often infeasible to deploy sensors capable of capturing every state variable. To address this limitation, a Koopman realization framework that relies solely on input-output data is required. This perspective is particularly important for industrial implementation. Moreover, prior research on Koopman operators using input-output data [2], [25], [28] has been limited, with most studies focusing exclusively on LTI Koopman formulations. Additionally, the selection of the arguments (i.e., embedded states) of the lifting function for controlled systems has not been thoroughly investigated.

Although modeling of diesel engine airpath systems has been widely investigated [29], [30], [31], achieving accurate and robust models remains highly challenging. These systems exhibit nonlinear and multivariable dynamics. The traditional approaches rely on physical modeling [30], often represented as linear parameter-varying (LPV) systems [32]. However, physical modelings suffer from limited accuracy and difficulties in parameter identification. In data-driven approaches, LTI modeling has been performed using ARX identification [33]; however, the applicability of LTI models is restricted due to the wide operating range of engines. For nonlinear system identification, studies such as [34] have adopted NARX-based methods, while the literature [29] employed a three-layer NN model. Although these nonlinear modeling approaches achieve high predictive performance, they pose challenges related to computational cost and training complexity.

C. Contribution and novelty

This paper presents a bilinear Koopman realization technique from input-output data, incorporating the optimization of the lifting function to enhance its applicability to industrial systems. In the proposed optimization algorithm, RBFs are employed as lifting functions, and their design parameters are optimized using a meta-heuristic approach, specifically PSO. The contributions and novelties of this paper are summarized as follows:

Bilinear Koopman realization from input-output data: For MIMO nonlinear systems, the prediction performance of an LTI Koopman realization is limited; therefore, a bilinear formulation is adopted for Koopman identification. In industrial applications, it is often the case that not all state variables can be measured and only input-output data are available, which is also assumed in this study. By incorporating time-delay coordinates into the measured input-output data and defining the input and output delays as embedded states, an input-output bilinear Koopman realization is constructed. For autonomous systems, it is natural that the embedded states are simply lifted since the states include only the output delays. For controlled systems, the selection of the embedded states lifted is important since the states include input delays in addition to output delays. Prior research (e.g., [2], [28]) employs just embedded states with outputs and inputs delay as arguments of lifting functions. However, the evolution of the inputs is not of interest from the perspective of system identification and feedback control. This is because the inputs are treated as exogenous signals supplied as random or feedback control inputs, rather than as variables evolving autonomously according to a dynamical flow. In this paper, we examine a proper selection of lifting arguments for input-output Koopman realizations. The proposed generalized bilinear Koopman realization solely from input-output data has not been considered in prior works.

Optimization of lifting function: The design of lifting functions significantly influences the prediction performance of Koopman realization and typically requires substantial manual effort [35]. In this study, RBFs are adopted as the lifting functions, and they are optimized using a metaheuristic approach based on multi-step prediction evaluation. This evaluation ensures high predictive accuracy of the Koopman model. The proposed approach has not been explored in prior research and offers several advantages: it does not require prior physical insight, leverages PSO as a well-established global optimization solver, and avoids the inherent challenges of neural network training. Compared to neural network training, PSO offers a robust global optimization framework with easier hyperparameter tuning, clearer objective function definition, and simpler implementation.

Application to the real-world industrial system: The proposed method is validated through its application to a diesel engine airpath system, which exhibits MIMO characteristics, strong interaction effects, and nonlinear behavior. The method provides a global bilinear formulation that achieves a balance between predictive accuracy and computational efficiency. This study represents the first application of Koopman-based modeling to a diesel engine airpath system, to the best of the

authors' knowledge. Accordingly, the proposed IO-Koopman modeling approach is verified through this real-world industrial application.

D. Article organization

This paper is organized as follows. Section II introduces the basic concept of the Koopman operator for input-dependent nonlinear systems, along with methods for representing LTI and bilinear systems using Koopman matrices with finite-dimensional approximations, and techniques for identifying these matrices. Section III proposes a hyperparameter identification method for RBFs, which are employed as lifting functions, in addition to input-output bilinear Koopman modeling. Sections IV and V evaluate the effectiveness of the proposed method through simulation and experimental tests, respectively. The controlled system is the intake and exhaust system of an internal combustion engine, which exhibits strong nonlinearity and MIMO characteristics common in industrial applications. Finally, Section VI summarizes the paper and discusses future research directions.

E. Notation

The symbol \mathbb{R}^n denotes the set of real numbers in n -dimensional space, and the symbol $\mathbb{R}^{n \times m}$ denotes the space of n -row and m -column matrices (or two-dimensional arrays) composed of real numbers. The symbols \mathcal{M} and \mathcal{N} denote smooth manifolds. The symbol \circ denotes function composition, the symbol \odot denotes the elementwise product, and the symbol \otimes denotes the Kronecker product. The symbol $\|\cdot\|_F$ denotes the Frobenius norm defined as $\|A\|_F = \sqrt{\sum_{i,j} a_{ij}^2}$, where a_{ij} is the element of matrix A . The symbol I_m denotes the identity matrix of size $m \times m$. The signal sequence is expressed as $(x_i)_{i=0}^\infty$. The space for all signal sequences is expressed as $\ell(\mathcal{X}) = \{(x_i)_{i=0}^\infty \mid x_i \in \mathcal{X}\}$. The map $\text{vec} : \ell(\mathcal{X}) \rightarrow \mathbb{R}^\infty$ converts a signal sequence to vectorized form. The symbol $0_{m \times n}$ is the zero matrix of size $m \times n$. The symbol \dagger denotes the Moore-Penrose pseudoinverse of a matrix. The notation $\psi_{[1:n]}$ is defined as $\psi_{[1:n]} = [\psi_1, \dots, \psi_n]^\top$, where $\psi_{[1:n]}$ is a vector-valued function composed of functions ψ_i for $i \in \{1, 2, \dots, n\}$.

II. DATA-DRIVEN MODELING VIA KOOPMAN OPERATOR

A. Koopman operator for non-autonomous system

We describe the Koopman operator theory for non-autonomous systems [2], [3], [4]. Consider a non-autonomous nonlinear system that includes control inputs:

$$x_{k+1} = f(x_k, u_k) \quad (1)$$

where $f : \mathcal{M} \times \mathcal{N} \rightarrow \mathcal{M}$ is the mapping, $x_k \in \mathcal{M} \subset \mathbb{R}^m$, $u_k \in \mathcal{N} \subset \mathbb{R}^m$ denotes the control input at time step k , and \mathcal{N} is a smooth manifold. For the system, an extended state is defined as

$$\chi_k = \begin{bmatrix} x_k \\ \nu_k \end{bmatrix} \quad (2)$$

where $\nu_k = \text{vec}((u_i)_{i=k}^\infty)$ denotes the state variable constructed from input sequences $(u_i)_{i=k}^\infty \in \ell(\mathcal{U})$. The dynamics of the system with the extended state are given as

$$\chi_{k+1} = F(\chi_k) = \begin{bmatrix} f(x_k, \nu_k(0)) \\ \mathcal{S}\nu_k \end{bmatrix} \quad (3)$$

where ν is the shift operator defined as $\mathcal{S}\nu_k = \nu_{k+1}$ and $\nu_k(0) = u_k$ denotes the first element of ν_k at time k . Therefore, the Koopman operator $\mathcal{K} : \mathcal{F} \rightarrow \mathcal{F}$ for nonlinear systems with inputs is defined as:

$$(\mathcal{K}\psi)(\chi_k) = \psi(F(\chi_k)). \quad (4)$$

The Koopman operator for controlled systems enables a nonlinear system to be represented in a (generally infinite-dimensional) linear form by lifting its state space to an infinite-dimensional space using the observable. The linearity of the Koopman operator helps the use of various linear control theories [2].

Remark 1. The manifolds \mathcal{M} and \mathcal{N} can be considered as $\mathcal{M} \subset \mathbb{R}^n$ and $\mathcal{N} \subset \mathbb{R}^m$ for most engineering problems [4], [20]. Actually, the states and inputs of the diesel engine airpath system are included in \mathbb{R}^n and \mathbb{R}^m , as shown in the simulation and experimental test sections.

B. Finite-dimensional Koopman operator

In Koopman operator theory, the operator acts on an infinite-dimensional space; therefore, for numerical computations, it is necessary to introduce a finite-dimensional approximation of the Koopman operator. In this section, we present the finite-dimensional approximation of the Koopman operator. The time evolution of a vector-valued lifting function $\psi : \mathbb{R}^n \times \mathbb{R}^m \rightarrow \mathbb{R}^{p+q}$ with $\psi \in \mathcal{F}$ is given as

$$\psi(x_{k+1}, u_{k+1}) = K \psi(x_k, u_k) \quad (5)$$

where $K \in \mathbb{R}^{(p+q) \times (p+q)}$ is the finite-dimensional Koopman matrix. The lifting function $\psi : \mathbb{R}^n \times \mathbb{R}^m \rightarrow \mathbb{R}^{p+q}$, which corresponds to the dictionary of observables, can be expressed using two lifting functions $\psi_x : \mathbb{R}^n \rightarrow \mathbb{R}^p$ and $\psi_u : \mathbb{R}^n \times \mathbb{R}^m \rightarrow \mathbb{R}^q$ as follows:

$$\psi(x_k, u_k) = \begin{bmatrix} \psi_x(x_k) \\ \psi_u(x_k, u_k) \end{bmatrix}. \quad (6)$$

Since the lifting function ψ_x depends on the state variables x , and ψ_u depends on both the state variables x and the input u , the generality is not lost [36]. Under this assumption, the time evolution of the lifting function using the finite-dimensional Koopman operator (i.e., the Koopman matrix K) is given as

$$\begin{bmatrix} \psi_x(x_{k+1}) \\ \psi_u(x_{k+1}, u_{k+1}) \end{bmatrix} = K \begin{bmatrix} \psi_x(x_k) \\ \psi_u(x_k, u_k) \end{bmatrix} = \begin{bmatrix} K_{11} & K_{12} \\ K_{21} & K_{22} \end{bmatrix} \begin{bmatrix} \psi_x(x_k) \\ \psi_u(x_k, u_k) \end{bmatrix} \quad (7)$$

where $K_{11} \in \mathbb{R}^{p \times p}$, $K_{12} \in \mathbb{R}^{p \times q}$, $K_{21} \in \mathbb{R}^{q \times p}$, and $K_{22} \in \mathbb{R}^{q \times q}$. Since we are interested in the time evolution of the states, the above equation can be simplified as follows:

$$\psi_x(x_{k+1}) = K_{11} \psi_x(x_k) + K_{12} \psi_u(x_k, u_k). \quad (8)$$

Previous studies [18], [19] have demonstrated that various system representations can be achieved by appropriately defining the lifting function $\psi_u(x_k, u_k)$.

1) *LTI Koopman form*: When representing the system in an LTI Koopman form, setting $\psi_u(x_k, u_k) = u_k$ yields the following LTI-Koopman form:

$$\psi_x(x_{k+1}) = K_{11} \psi_x(x_k) + K_{12} u_k. \quad (9)$$

Here, let $A = K_{11}$, $B = K_{12}$, and $z_k = \psi_x(\cdot)$. Then, the LTI state-space equation for lifted states z_k is given as

$$z_{k+1} = Az_k + Bu_k. \quad (10)$$

2) *Bilinear Koopman form*: According to the literature [18], [22], a bilinear Koopman form can be expressed by defining the lifting function $\psi_u : \mathbb{R}^n \times \mathbb{R}^m \rightarrow \mathbb{R}^{m+mp}$ as follows:

$$\psi_u(x_k, u_k) = \begin{bmatrix} u_k \\ \psi_x(x_k) \otimes u_k \end{bmatrix} \quad (11)$$

where $\psi_x(x_k) \otimes u_k$ is calculated as

$$\psi_x(x_k) \otimes u_k = [u_k(1)\psi_x(x_k), u_k(2)\psi_x(x_k), \dots, u_k(m)\psi_x(x_k)]^\top \in \mathbb{R}^{mp}. \quad (12)$$

Then, the time evolution of the lifting functions is expressed as

$$\begin{bmatrix} \psi_x(x_{k+1}) \\ u_{k+1} \\ \psi_x(x_{k+1}) \otimes u_{k+1} \end{bmatrix} = \begin{bmatrix} A & B_0 & B \\ * & * & * \\ * & * & * \end{bmatrix} \begin{bmatrix} \psi_x(x_k) \\ u_k \\ \psi_x(x_k) \otimes u_k \end{bmatrix} \quad (13)$$

where $A \in \mathbb{R}^{p \times p}$, $B_0 \in \mathbb{R}^{p \times m}$, $B = [B_1, \dots, B_m] \in \mathbb{R}^{p \times mp}$, and $B_i \in \mathbb{R}^{p \times p}$ ($i = 1, \dots, m$). Since we are interested in the time evolution of the states and not in the time evolution of the inputs, the elements of the Koopman matrix related to the input dynamics can be ignored. Therefore, the above equation (13) is reduced to

$$\psi_x(x_{k+1}) = A\psi_x(x_k) + B_0 u_k + B(\psi_x(x_k) \otimes u_k). \quad (14)$$

Let $z_k = \psi_x(\cdot)$ denote the lifted state at time k . Then, the bilinear state equation can be written in the following form:

$$z_{k+1} = Az_k + B_0 u_k + B(z_k \otimes u_k). \quad (15)$$

C. Learning of Koopman matrix

For a nonlinear system with inputs, we assume to measure time-series data of the measurable state variables x_k , and the inputs u_k are collected, i.e., $\mathcal{D} = \{(x_k, u_k) \mid k = 1, \dots, N_d\}$. From the dataset, the snapshot data are set as: Z^+ and Z_w are given as

$$Z^+ = [z_2, z_3, \dots, z_{N_d}]$$

$$Z_w = \begin{bmatrix} z_1 & z_2 & \dots & z_{N_d-1} \\ w_1 & w_2 & \dots & w_{N_d-1} \\ z_1 \otimes w_1 & z_2 \otimes w_2 & \dots & z_{N_d-1} \otimes w_{N_d-1} \end{bmatrix}. \quad (16)$$

Then, the state-space matrices A , B_0 , B for the bilinear Koopman realization are obtained from the following optimization problem:

$$\min_H \|Z^+ - H Z_w\|_F \quad (17)$$

where $H = [A, B_0, B] \in \mathbb{R}^{p \times p(m+l+1)}$. This least-squares problem can be solved using the Moore-Penrose pseudoinverse as follows:

$$H = Z^+ [Z_w, U]^\dagger. \quad (18)$$

In the case of a linear system, the elements of the bilinear term are removed from the snapshot data.

III. PROPOSED METHODOLOGY

A. Time-delay coordinates

We explain input-output Koopman modeling [2], which addresses the case where only input-output data can be measured while the system states are unknown or unobservable. Since the diesel engine airpath system which has exogenous inputs is considered in this paper, this section handles the nonlinear system with control and exogenous inputs, given as

$$\begin{aligned} x_{k+1} &= f(x_k, u_k, d_k) \\ y_k &= h(x_k, u_k, d_k) \end{aligned} \quad (19)$$

where $d_k \in \mathbb{R}^l$ is the measurable exogenous input, $y_k \in \mathbb{R}^{n_h}$ is the measurable output, and $f : \mathbb{R}^n \times \mathbb{R}^m \times \mathbb{R}^l \rightarrow \mathbb{R}^n$, $h : \mathbb{R}^n \times \mathbb{R}^m \times \mathbb{R}^l \rightarrow \mathbb{R}^{n_h}$. For this system with inputs, we assume to obtain the dataset: $\mathcal{D} = \{y_k, w_k \mid k = 1, \dots, N_d\}$, where w_k is defined as $w_k = [u_k \ d_k]^\top$. The time-delay coordinates are introduced to address the constraint that only input-output data can be measured. The *embedded* state at time k , considering delay-step n_d , is defined as:

$$\zeta_k = [(\zeta_k^y)^\top \ (\zeta_k^w)^\top]^\top \in \mathbb{R}^{n_\zeta} \quad (20)$$

with

$$\zeta_k^y = [y_k^\top \ y_{k-1}^\top \ \dots \ y_{k-n_d}^\top]^\top \in \mathbb{R}^{(n_d+1)n_h} \quad (21)$$

$$\zeta_k^w = [w_{k-1}^\top \ w_{k-2}^\top \ \dots \ w_{k-n_d}^\top]^\top \in \mathbb{R}^{n_d(m+l)} \quad (22)$$

where $n_\zeta = n_d(n_h + m + l)n_h$.

B. IO generalized bilinear Koopman form

As well as Section II-B, the Koopman model is given as

$$\psi_x(\zeta_{k+1}) = K_{11}\psi_x(\zeta_k) + K_{12}\psi_w(\zeta_k) \quad (23)$$

where the lifting function $\psi_w : \mathbb{R}^{n_\zeta} \times \mathbb{R}^{n_d(m+l)} \rightarrow \mathbb{R}^{(m+l)+(m+l)q}$ is defined as:

$$\psi_w(\zeta_k, w_k) = \begin{bmatrix} w_k \\ \phi_w(\zeta_k) \otimes w_k \end{bmatrix} \quad (24)$$

where $\phi_w : \mathbb{R}^{n_\zeta} \rightarrow \mathbb{R}^{n_w}$ is the function. Then, analogous to (13), the standard form is formulated as

$$\begin{bmatrix} \psi_x(\zeta_{k+1}) \\ w_{k+1} \\ \phi_w(\zeta_{k+1}) \otimes w_{k+1} \end{bmatrix} = \begin{bmatrix} A & B_0 & B \\ * & * & * \\ * & * & * \end{bmatrix} \begin{bmatrix} \psi_x(\zeta_k) \\ w_k \\ \phi_w(\zeta_k) \otimes w_k \end{bmatrix} \quad (25)$$

Since the time evolution of interest corresponds to the embedded states, the above equation is simplified as:

$$\psi_x(\zeta_{k+1}) = A\psi_x(\zeta_k) + B_0 w_k + B(\phi_w(\zeta_k) \otimes w_k). \quad (26)$$

By defining $z_{w,k} = \phi_w(\cdot)$, the generalized bilinear forms can be rewritten by

$$z_{k+1} = Az_k + B_0w_k + B(z_{w,k} \otimes w_k). \quad (27)$$

Remark 2. The IO generalized bilinear Koopman form (26) can be viewed as a bilinear-like LPV Koopman realization by considering $\phi_w(\zeta_k)$ as a scheduling function.

C. Argument selection of lifting function for IO-Koopman realization

The lifting function in previous studies on the standard IO-Koopman form is defined as

$$\psi_x(\zeta_k) = \begin{bmatrix} \zeta_k \\ \psi_{[1:n_l]}(\zeta_k) \end{bmatrix} \in \mathbb{R}^{n_\zeta + n_l} \quad (28)$$

where $\psi_{[1:n_l]} = [\psi_1, \dots, \psi_{n_l}]^\top$, and ψ_i is a scalar function for $i \in \{1, \dots, n_l\}$. In previous IO-Koopman realization [2], the lifting function is typically chosen as $\psi_i(\zeta_k)$. Under this lifting function setting, if $\psi(\zeta_k) = [y_k, w_{k-1}, w_{k-1} \odot w_{k-1}]^\top$ is given, the time evolution of $\psi(\zeta_k)$ includes inputs. However, we are not interested in predicting observables that include inputs, since inputs are externally provided—either randomly or through a control law. Thus, employing $\psi(\zeta_k)$ may result in the failure of capturing the essential system dynamic characteristics due to spurious dynamics of exogenous input, which deteriorate the prediction performance or require a significantly larger amount of training data. Although infinite input sequences are assumed in previous research, it is not feasible to cover all possible input sequences due to the finite amount of data in practical situations. Therefore, unlike prior studies [2], [28], we propose explicitly excluding w_k from nonlinear lifting to prevent the identification of spurious dynamics induced by exogenous inputs. Specifically, we propose the following observable selection:

$$\psi_x(\zeta_k) = \begin{bmatrix} \zeta_k \\ \psi_{[1:n_l]}(\zeta_k^y) \end{bmatrix} \in \mathbb{R}^{n_\zeta + n_l}. \quad (29)$$

Then, the IO bilinear Koopman model is expressed as (30) shown at the bottom of the page. This formulation indicates that the embedded state with input delay is generated by a given input. In other words, the input after transitions, w_k , is included in the time-evolved state $z_{k+1} (= \psi_x(\zeta_{k+1}^y))$ and

the input delay is generated through this input transition. Therefore, the matrices A and B associated with the input-output delay transition are trivially determined by the shift relationship. If there is an observable associated with the input (e.g., $y_k \odot w_{k-1} \odot w_{k-1}$), the observable is not generated from the given input w_k . Thus, the matrix $A_{\psi\star\star}$ in the Koopman matrix A associated with the time evolution of the lifted state is not uniquely determined. Therefore, in this study, the argument of ψ_i is ζ_k^y instead of ζ_k . On the other hand, because ϕ_w does not contribute to the time evolution of $\psi_x(\zeta_k)$, we employ a lifting function related to ζ_k to increase the flexibility of our representation:

$$\phi_w(\zeta_k) = [\phi_{[1:n_w]}(\zeta_k)] \in \mathbb{R}^{n_w} \quad (31)$$

where $\phi_i : \mathbb{R}^{n_\zeta} \rightarrow \mathbb{R}$ for $i \in \{1, \dots, n_w\}$. The output equation is also given as $y_k = Cz_k$ with $C = [I_{n_h} \ 0_{n_h \times (n_l - n_h)}]$. We summarize the above discussion as follows:

Theorem 1. Consider the IO generalized bilinear Koopman realization (26) with the state-transition structure in (30), where $z_k (= \psi_x(\cdot))$ represents “state” variables updated by a time-invariant linear map A , and the new input w_k is injected via B_0 and B . Suppose that ψ_x contains an input-dependent nonlinear component $\psi_i(\zeta_k)$, such as $w_{k-1} \odot w_{k-1}$ or $y_k \odot w_{k-1}$. Then the next-time quantity $g_{k+1} (= \psi_i(\zeta_{k+1}))$ corresponding to ψ_i generally depends on the new input w_k , and it is structurally impossible to generate g_{k+1} by the block $A_{\psi\star\star}$, and including such nonlinearities in ψ_x is causally inconsistent with (30).

Proof: Assume $g_{k+1} = a^\top z_k$, where a^\top is the row of $A_{\psi\star\star}$ corresponding to the observable ψ_i . Fix ζ_k (thus z_k) and choose $w_k^{(1)} \neq w_k^{(2)}$. Since g_{k+1} depends on w_k (e.g., $y_{k+1} \odot w_k$), one obtains $g_{k+1}^{(1)} \neq g_{k+1}^{(2)}$, whereas $a^\top z_k$ is identical for both choices (\because it contains no w_k). This contradiction proves that g_{k+1} cannot be produced by $A_{\psi\star\star}$. ■

Remark 3. Theorem 1 indicates that using $\psi_i(\zeta_k)$ may prevent the essential system dynamics from being captured due to spurious dynamics induced by the exogenous input.

Corollary 1. To preserve causal consistency with the state-transition structure in (30), input-dependent nonlinearities must be allocated to $\phi_w(\zeta_k)$, and the arguments of ψ_i should be restricted to ζ_k^y .

$$\begin{bmatrix} y_{k+1} \\ y_k \\ \vdots \\ y_{k-n_d+1} \\ w_k \\ w_{k-1} \\ \vdots \\ w_{k-n_d+1} \\ \psi_{[1:n_l]}(\zeta_{k+1}^y) \end{bmatrix} = \begin{bmatrix} A_{yy1} & A_{yy2} & \cdots & A_{yyn_d} & A_{yw1} & A_{yw2} & \cdots & A_{yw_{n_d}} & A_{y\psi} \\ I & 0 & 0 & 0 & 0 & 0 & 0 & 0 & 0 \\ 0 & \ddots & 0 & \ddots & 0 & 0 & 0 & 0 & 0 \\ 0 & 0 & I & 0 & 0 & 0 & 0 & 0 & 0 \\ 0 & 0 & 0 & 0 & 0 & 0 & 0 & 0 & 0 \\ 0 & 0 & 0 & 0 & 0 & 0 & 0 & 0 & 0 \\ \vdots & \vdots & \ddots & \ddots & \vdots & 0 & \ddots & 0 & 0 \\ 0 & 0 & 0 & 0 & 0 & 0 & I & 0 & 0 \\ A_{\psi y1} & A_{\psi y2} & \cdots & A_{\psi y_{n_d}} & A_{\psi w1} & A_{\psi w2} & \cdots & A_{\psi w_{n_d}} & A_{\psi\psi} \end{bmatrix} \begin{bmatrix} y_k \\ y_{k-1} \\ \vdots \\ y_{k-n_d} \\ w_{k-1} \\ w_{k-2} \\ \vdots \\ w_{k-n_d} \\ \psi_{[1:n_l]}(\zeta_k^y) \end{bmatrix} + \begin{bmatrix} 0 \\ 0 \\ \vdots \\ 0 \\ 0 \\ 0 \\ \vdots \\ 0 \\ 0 \end{bmatrix} + B(\phi_w(\zeta_k) \otimes w_k) \quad (30)$$

Proof: According to Theorem 1, placing input nonlinearities inside ψ_x forces their next-time image to depend on w_k , which cannot be realized by the state-transient matrix A . Thus, to preserve the interpretation that ψ_x represents state variables updated solely by A , input-dependent nonlinearities should be handled through $\phi_w(\zeta_k)$ so that their w_k -dependence is routed via B_0 and B , while ψ_x is restricted to ζ_k^y . \blacksquare

D. IO generalized Koopman realization

This section describes IO generalized bilinear Koopman realization. The snapshot data for the extended states and inputs are set as

$$X = [\zeta_1, \zeta_2, \dots, \zeta_{N_d-n_d}] \quad (32)$$

$$W = [w_1, w_2, \dots, w_{N_d-n_d}] \quad (33)$$

with

$$\zeta_i = [\zeta_i^y \quad \zeta_i^w]^\top \in \mathbb{R}^{n_\zeta} \quad (34)$$

$$\zeta_i^y = [y_{i,n_d}^\top \quad y_{i,n_d-1}^\top \quad \dots \quad y_{i,0}^\top]^\top \in \mathbb{R}^{(n_d+1)n_d} \quad (35)$$

$$\zeta_i^w = [w_{i,n_d-1}^\top \quad w_{i,n_d-2}^\top \quad \dots \quad w_{i,0}^\top]^\top \in \mathbb{R}^{n_d(m+l)}. \quad (36)$$

Then, the snapshot data Z^+ and Z_w for IO generalized koopman realization are expressed as

$$Z^+ = [z_2, z_3, \dots, z_{N_d}]$$

$$Z_w = \begin{bmatrix} z_1 & z_2 & \dots & z_{N_d-1} \\ w_1 & w_2 & \dots & w_{N_d-1} \\ z_{w,1} \otimes w_1 & z_{w,2} \otimes w_2 & \dots & z_{w,N_d-1} \otimes w_{N_d-1} \end{bmatrix} \quad (37)$$

and, the IO generalized bilinear Koopman model is obtained from the optimization probelm (17).

E. Optimization of lifting functions

This section presents the optimization method of lifting functions. Herein, we optimize the design parameters of RBFs. The lifting function is generally selected, such as mechanics-inspired selection, empirical selection (e.g., monomials, polynomials), and RBF selection with randomly selected design parameters. Such selections may not provide good performance since the lifting function is not optimized. The finding method of the proper lifting function is mainly a NN-based approach. This approach has the same difficulties as general NN learning, including hyperparameter setting, overfitting, model complexity, computational cost, vanishing and exploding gradient problem. In this paper, we adopt a metaheuristic optimization (e.g., PSO) approach, as an alternative approach to the NN-based method.

The optimization algorithm is shown in Algorithm 1. In the proposed optimization method, RBFs are adopted as the lifting functions. For example, polyharmonic RBFs are given as

$$\psi(x_1; \theta_1) = \|x_1 - \theta_1\|_2 \log \|x_1 - \theta_1\|_2 \quad (38)$$

$$\phi(x_2; \theta_2) = \|x_2 - \theta_2\|_2 \log \|x_2 - \theta_2\|_2 \quad (39)$$

where x_i and θ_i ($i = 1, 2$) are the input and center vectors of the RBFs. The center is considered the design parameter. Then, the design parameters of the RBFs are optimized by global optimization such as PSO.

Algorithm 1 Optimization of lifting functions

```

1: Inputs:
2:   Max iteration  $N_{\max}$ 
3:   RBFs  $\psi(x_1; \theta_1)$ ,  $\phi(x_2; \theta_2)$ 
4:   Dataset  $\mathcal{D} = \{y_k, u_k, d_k \mid k = 1, \dots, N_d\}$ 
5: Outputs:
6:   Design parameter vector  $\theta = [\theta_1, \theta_2]$ 
7:   Koopman matrices  $A, B_0, B, C$ 
8:   Set initial  $\theta$ , Maximum iterations  $N_{\max}$ 
9:    $iteration \leftarrow 1$ 
10:  while ( $iteration \leq N_{\max}$ ) do
11:    Compute Koopman matrices  $A, B_0, B, C$  for  $\psi(x_1; \theta_1), \phi(x_2; \theta_2)$  via Koopman realization
12:    Update  $\theta$  by minimizing  $J(\theta)$ 
13:    if  $J(\theta) < \varepsilon$  then
14:      break
15:    end if
16:     $iteration \leftarrow iteration + 1$ 
17:  end while
18:  Return  $\theta^* = \arg \min J(\theta)$  and matrices  $A, B_0, B, C$ 

```

As shown in Algorithm 1, the proposed optimization process of the centers of RBFs encompasses the realization of the Koopman matrix. The optimization problem is formulated as

$$\min_{\theta} J(\theta), \quad J(\theta) = \sum_{k=1}^{N_d} (y_k - \hat{y}_k(\theta))^2 \quad (40)$$

where \hat{y}_k denotes *multi-step (not one-step)* prediction given by

$$\begin{cases} \hat{z}_{k+1} = A\hat{z}_k + B_0 w_k + B(\hat{z}_{w,k} \otimes w_k) \\ \hat{y}_k = C\hat{z}_k \end{cases} \quad (41)$$

with the initial lifted states $z_0 = \psi(\zeta_0)$ and $z_{w,0} = \phi(\zeta_0)$. Matrices A, B_0, B, C can be obtained by Koopman realization for candidate centers, as shown in Section III-D.

F. Model validation

In model validation, the modeling accuracy is evaluated using the coefficient of determination, R^2 , of y , defined as

$$R^2 = 1 - \frac{\sum_{k=1}^{N_d} (y_k - \hat{y}(k))^2}{\sum_{k=1}^{N_d} (y(k) - \bar{y})^2} \quad (42)$$

where \bar{y} is the mean value of the N_d data [37]. An R^2 score equal to 1.0 indicates that the identified model best fits the target system. From an engineering perspective, an R-squared score is acceptable when it reaches a value from 0.9 to 1.0 [38]. A negative value means that the inferred model has a very low ability to represent an equivalent dynamical system. In nonlinear systems, multi-step prediction may not be achievable even when accurate one-step prediction is achieved [39]. Therefore, we evaluate both one-step and multi-step predictions. The one-step prediction is defined as

$$\begin{cases} \hat{x}(t+1) = f(x(t), u(t), d(t)) \\ \hat{y}(t) = h(\hat{x}(t)) \end{cases} \quad (43)$$

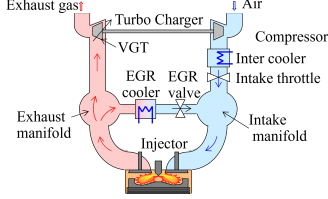


Fig. 1. Diesel engine airpath system.

where \hat{y} is the predicted value of y . The one-step ahead is predicted from the given input and output data. The multi-step prediction is defined as

$$\begin{cases} \hat{x}(t+1) = f(\hat{x}(t), u(t), d(t)) \\ \hat{y}(t) = h(\hat{x}(t)) \end{cases} \quad (44)$$

with $\hat{x}(0) = x(0)$. The multi-step ahead is predicted from the given input and the predicted past output.

IV. SIMULATION

A. Target system

The intake and exhaust system of a four-cylinder diesel engine [35] is shown in Fig. 1. This system includes an exhaust gas recirculation (EGR) system and a variable geometry turbocharger (VGT). The EGR system regulates the oxygen concentration entering the cylinders by mixing oxygen-lean exhaust gas with fresh air. This reduces the oxygen concentration, lowers the peak combustion temperature, and suppresses the formation of harmful nitrogen oxides, which are produced in large quantities at high temperatures. The VGT system adjusts the pressure inside the intake manifold. By narrowing the spacing of the movable vanes, the flow path is restricted and the flow rate increases, achieving a supercharging effect even at low engine speeds. At high engine speeds, the vane spacing is widened to facilitate exhaust gas flow. Fresh air is drawn in from the atmosphere and compressed by the compressor. After cooling in the intercooler, it passes through the intake throttle and enters the intake manifold. Exhaust gas also flows into the intake manifold after passing through the EGR valve. The oxygen concentration in the intake manifold is controlled by operating the EGR valve. The mixture then flows into the cylinders, and after combustion, the exhaust gas is discharged into the exhaust manifold. The gas leaving the exhaust manifold splits into two paths: one recirculated through the EGR cooler, and the other passing through the turbine and exiting as exhaust gas. The burned gas drives the turbine, and the turbine speed is controlled by adjusting the vane angle. In this study, modeling is performed using a data-driven approach; therefore, further explanation of physical modeling is omitted. For details, refer to [40].

B. Simulation setting

Training and test data were generated using a design of experiments (DoE). Refer to [35], [41]. The generated input signals were applied to the plant inputs (i.e., VGT valve position, EGR valve position, fuel injection amount, and engine speed), and the outputs (i.e., intake manifold pressure

TABLE I
SIMULATION CASES OF KOOPMAN REALIZATION.

Case	Lifting function ψ_x	Lifting function ϕ_w	Opt.
H-DMD	ζ_k	—	—
LK	$\begin{bmatrix} \zeta_k \\ \psi_{[1:10]}(\zeta_k) \end{bmatrix}$	—	with
BLK(poly)	10th-order polynomial of ζ_k	Similar to ψ_x	—
BLK	$\begin{bmatrix} \zeta_k \\ \psi_{[1:10]}(\zeta_k) \end{bmatrix}$	Similar to ψ_x	with
GBLK	$\begin{bmatrix} \zeta_k \\ \psi_{[1:5]}(\zeta_k^y) \end{bmatrix}$	$\begin{bmatrix} \zeta_k \\ \phi_{[1:5]}(\zeta_k) \end{bmatrix}$	with

and EGR rate) were measured. The sampling period was set to 0.1 seconds, resulting in 25,000 data points. The time-series data were normalized as a preprocessing step. To optimize the RBF hyperparameters, PSO, a reliable global optimization solver, was employed. A delay step of 2 was used. PSO was implemented using the MATLAB's particleswarm function with a maximum of 30 iterations and a swarm size of 300. Parallel computation was also utilized. Table I shows the koopman forms considered. The number of optimization parameters was set to 10 for all cases. In the table, H-DMD represents Hankel-DMD [42]: $z_{k+1} = Az_k + B_w w_k$, LK represents the LTI Koopman realization [2], [14]: $z_{k+1} = Az_k + B_w w_k$, BLK represents the standard bilinear Koopman realization [18], [35]: $z_{k+1} = Az_k + B_w w_k + B_z(z_k \otimes w_k)$, GBLK represents the generalized bilinear Koopman realization (the proposed method): $z_{tk+1} = Az_t + B_w w_t + B_z(z_{w,k} \otimes w_k)$.

C. Results and discussions

Fig. 2 illustrates the training and test data generated by applying input signals and measuring the corresponding outputs. The orange and blue lines represent the training and test datasets, respectively. In the figure, y_1 , y_2 , u_1 , u_2 , d_1 , and d_2 denote the intake manifold pressure [kPa], EGR rate [%], VGT vane position [%], EGR valve position [%], fuel injection amount [mm^3/st], and engine speed [rpm], respectively. Fig. 3 presents the time-series data of prediction performance for test data. The dotted lines represent the predicted values, and the solid lines represent actual values. Table II reports the R-squared scores for one-step and long-term predictions for the above cases. We compared our method with conventional approaches, including Hankel DMD, the LTI Koopman model, the bilinear Koopman model with polynomial basis functions, and the bilinear Koopman model with randomly assigned RBF centers. Among these, Hankel DMD without lifting exhibited the poorest predictive performance, and the LTI Koopman model without RBF optimization also performed poorly. Although RBF optimization significantly improved the predictive accuracy of the LTI Koopman model, the improvement was still insufficient, highlighting the need for identification in the bilinear model. Next, we examined the case where the lifting function for the bilinear form was polynomial and found that its predictive performance was substantially poor. For the standard bilinear form, the R^2 value exceeded 0.8 after RBF optimization. However, increasing the number of RBFs led to a marked deterioration in predictive performance on the

TABLE II
R-SQUARED OF ONE-STEP AND LONG-TERM PREDICTIONS IN THE SIMULATION.

Case	One-step prediction		Long-term prediction			
	learning data	test data	learning data	test data	y_1	y_2
H-DMD	0.994	0.991	-14.5	-7.85	-15.0	-7.89
LK	0.992	0.989	0.793	0.910	0.778	0.908
BLK(poly)	0.996	0.993	-14.3	-7.77	-14.8	-7.78
BLK	0.996	0.993	0.874	0.988	-0.295	0.347
GBLK	0.995	0.992	0.931	0.951	0.922	0.949

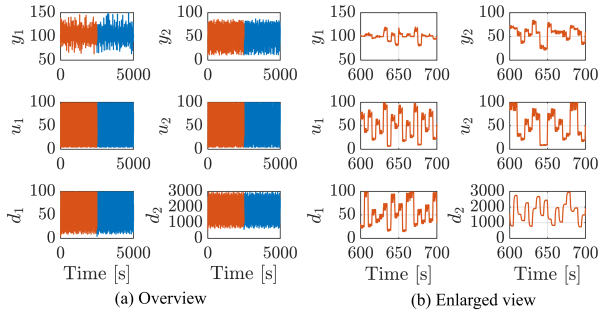


Fig. 2. The learning and test data in simulation.

test data, indicating poor generalization. This is likely due to the inclusion of inputs in the observables, as discussed in Section III-D. Finally, the proposed generalized bilinear form B with RBF optimization achieved the highest prediction accuracy in this study, with an R^2 value of over 0.9, meeting the requirements for engineering applications [38].

Simulation results demonstrated that the proposed method significantly outperformed conventional approaches. The predicted output of the linearly identified model exhibited poor long-term predictive performance in ODE simulations. Diesel engine airpath systems exhibit complex nonlinear characteristics, yet linear models and Hankel DMD rely on linear realizations and therefore fail to deliver satisfactory results. We then examined the bilinear Koopman realization. First, for the bilinear Koopman model using polynomial basis functions—similar to previous studies [24], [25]—the lifting functions were selected based on findings from SINDy modeling [35]. However, this approach proved ineffective for modeling diesel engine airpath systems. Since designers cannot successfully reuse the basis functions employed in SINDy, alternative approaches are required. Previous literature has used randomly centered RBFs as lifting functions, but as noted in [43], Koopman models with non-optimized RBFs tend to diverge. Our simulations confirmed this observation: while one-step predictions achieved very high R^2 exceeding 0.98, long-term predictions failed to meet performance requirements. Our proposed method addresses this issue by optimizing the centers of the RBFs used as lifting functions based on multi-step prediction performance. The bilinear Koopman model with RBF optimization demonstrated superior predictive accuracy compared to other methods. Furthermore, we confirmed that prediction and generalization performance depend strongly on the choice of arguments for the lifting function. Previous studies typically used embedded state variables consisting of

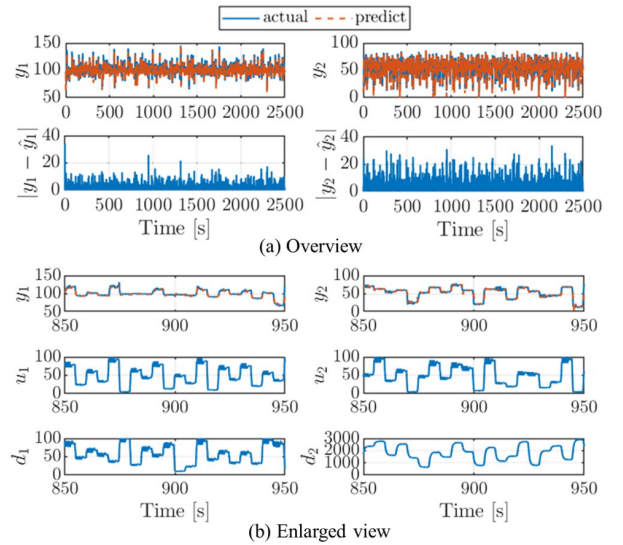


Fig. 3. The long-term predictive performance of y_1 and y_2 for test data in simulation.

time delays of inputs and outputs, but we found that these methods suffered from poor prediction and generalization. In contrast, our proposed argument selection strategy achieved significantly better performance. These results demonstrate the effectiveness of the proposed method.

V. REAL-WORLD EXPERIMENTAL VERIFICATION

A. Experimental setting

A real-world engine bench test, as shown in Fig. 4, was conducted. The experimental environment is the same as in the literature [44]. The variable y_2 represents the mass air flow (MAF) [mg/st], which is related to the EGR ratio, while the other variables are the same as those used in the simulation. In the engine bench tests, training and test data are collected under closed-loop conditions. The sampling period was 100 ms. In contrast, the simulation section used open-loop data, which are generally considered preferable. Here, we demonstrate that the proposed method remains effective in closed-loop experiments, where measurement noise tends to be amplified. The controller employed in the closed-loop experiments was a PID-based mass-production controller.

B. Results and discussions

Fig. 5 shows the learning and test data. The Koopman models were derived from the learning data. Fig. 6 shows the

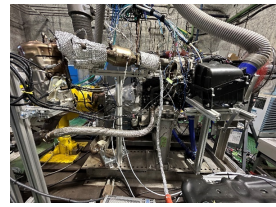


Fig. 4. Engine bench test. Fuel type:diesel, Arrangement cylinders: 4 in line, Maximum power:110 kW (150 PS)3600 rpm, Maximum torque: 350 Nm (35.69 kgm)1800-2600 rpm (net), Combustion type: Direct injection with water-cooled 4-valve DOHC (double overhead camshaft).

TABLE III

R-SQUARED OF ONE-STEP AND LONG-TERM PREDICTIONS IN THE EXPERIMENTAL TEST.

Case	One-step prediction		Long-term prediction			
	learning data		learning data		test data	
	y_1	y_2	\hat{y}_1	\hat{y}_2	y_1	y_2
LK	0.999	0.994	0.988	0.973	0.917	0.834
BKL	0.999	0.997	0.997	0.992	-0.774	-3.68
GBKL	0.999	0.997	0.996	0.992	0.936	0.911

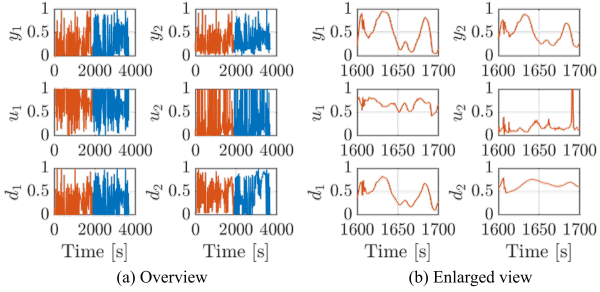


Fig. 5. The learning and test data in experimental test.

prediction performance of the proposed method on the test data. These signals are normalized. In addition, we compare the performance of the conventional and proposed methods. Table III reports the R-squared values for one-step predictions on the learning data and for both one-step and long-term predictions on the test data. The table also compares the results of the linear and bilinear Koopman realizations. The cases presented in Table III corresponds to those shown in Table I. From the results, the proposed method provides the best performance among them, as well as simulation verification. The LTI Koopman form is limited to the prediction performance. The predictions of the standard bilinear Koopman form, where lifting functions are $\psi_x = \psi_w$ diverge for the test data. However, the proposed generalized bilinear Koopman form provides the desired performance for learning and test data. From the above, the effectiveness of the proposed methodology was experimentally verified.

Section V has examined the effectiveness of the proposed method through an actual engine bench test. Similar to the simulation verification, the proposed method—namely, the IO bilinear Koopman realization—achieves the best performance among the compared methods, including the LTI Koopman realization and the standard bilinear Koopman realization. In the simulation section, the learning data were acquired through an open-loop test. General system identification typically prefers rich excitation signals under open-loop testing conditions. In the experimental section, we assumed a more realistic scenario and obtained transient data from closed-loop experiments as training data. In other words, we considered that in actual tests, applying random vibrations using open-loop tests would not be easy and would require additional technical expertise. Even under such conditions, we demonstrated that the proposed method can achieve the desired results for both the training and test data.

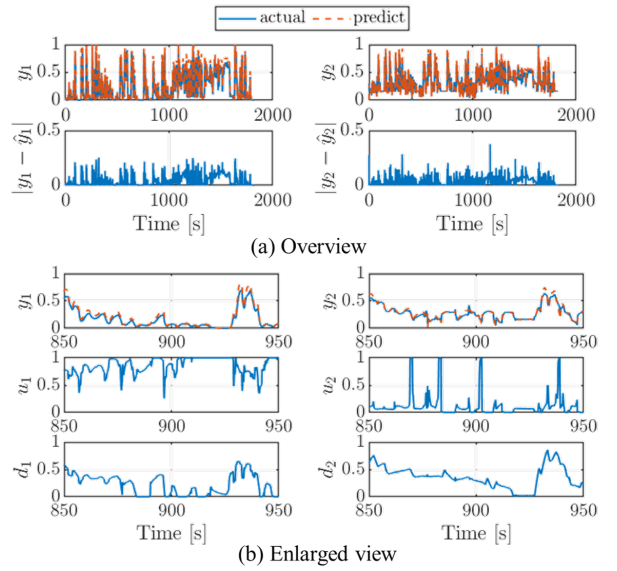


Fig. 6. The long-term predictive performance of y_1 and y_2 for test data in experimental test.

VI. CONCLUSIONS

This study presented an input-output bilinear Koopman realization with a lifting function optimization algorithm. The proposed framework integrates bilinear Koopman realization, input-output data utilization, and lifting function optimization. This approach enables Koopman-based modeling under practical constraints where only input-output data are available, significantly expanding its applicability to industrial systems. The key contributions of this work include the investigation of bilinear form structures for Koopman realization, the systematic selection of lifting function arguments when using input-output data, the optimization of lifting functions via PSO, and the successful application of the proposed method to an industrial diesel engine airpath system. Unlike previous studies that simply combined embedded states with input and output delays—thus including the time evolution of uninformative inputs—our method addresses argument selection to enhance predictive performance. Furthermore, because the design of the lifting function strongly influences accuracy and is difficult for users to determine, the proposed PSO-based optimization—where the centers of the RBFs employed as the lifting function are optimized—provides a practical and effective solution. The method was validated on a diesel engine intake and exhaust system exhibiting strong nonlinearity and MIMO characteristics. Simulation and experimental test results demonstrated substantial improvements in predictive accuracy compared to conventional approaches, achieving an R-squared over 0.90, which meets engineering requirements. Future work will focus on constructing controller with IO Koopman model.

REFERENCES

- [1] P. Van Overschee and B. De Moor, “N4SID: Subspace algorithms for the identification of combined deterministic-stochastic systems,” *Automatica*, vol. 30, no. 1, pp. 75–93, Jan. 1994.
- [2] M. Korda and I. Mezić, “Linear predictors for nonlinear dynamical systems: Koopman operator meets model predictive control,” *Automatica*, vol. 93, pp. 149–160, July 2018.

[3] M. O. Williams, C. W. Rowley, and I. G. Kevrekidis, "A kernel-based method for data-driven koopman spectral analysis," *Journal of Computational Dynamics*, vol. 2, no. 2, pp. 247–265, 2015.

[4] J. L. Proctor, S. L. Brunton, and J. N. Kutz, "Generalizing Koopman Theory to Allow for Inputs and Control," *SIAM Journal on Applied Dynamical Systems*, vol. 17, no. 1, pp. 909–930, Jan. 2018.

[5] K. Huang, K. Wei, F. Li, C. Yang, and W. Gui, "LSTM-MPC: A Deep Learning Based Predictive Control Method for Multimode Process Control," *IEEE Transactions on Industrial Electronics*, vol. 70, no. 11, pp. 11 544–11 554, Nov. 2023.

[6] K. Zhang, X. Luan, F. Ding, and F. Liu, "A Bayesian transfer sparse identification method for nonlinear ARX systems," *International Journal of Adaptive Control and Signal Processing*, vol. 38, no. 10, pp. 3484–3502, Oct. 2024, publisher: Wiley.

[7] S. L. Brunton, J. L. Proctor, and J. N. Kutz, "Sparse Identification of Nonlinear Dynamics with Control (SINDyC)," May 2016, arXiv:1605.06682 [math].

[8] D. Bhattacharya, R. Hashem, L. K. Cheng, and W. Xu, "Nonlinear Model Predictive Control of a Robotic Soft Esophagus," *IEEE Transactions on Industrial Electronics*, vol. 69, no. 10, pp. 10 363–10 373, Oct. 2022.

[9] S. L. Brunton, M. Budišić, E. Kaiser, and J. N. Kutz, "Modern Koopman Theory for Dynamical Systems," *SIAM Review*, vol. 64, no. 2, pp. 229–340, May 2022.

[10] P. Bevanda, S. Sosnowski, and S. Hirche, "Koopman Operator Dynamical Models: Learning, Analysis and Control," *Annual Reviews in Control*, vol. 52, pp. 197–212, 2021.

[11] P. J. Schmid, "Dynamic mode decomposition of numerical and experimental data," *Journal of Fluid Mechanics*, vol. 656, pp. 5–28, Aug. 2010.

[12] J. L. Proctor, S. L. Brunton, and J. N. Kutz, "Dynamic Mode Decomposition with Control," *SIAM Journal on Applied Dynamical Systems*, vol. 15, no. 1, pp. 142–161, Jan. 2016.

[13] M. O. Williams, I. G. Kevrekidis, and C. W. Rowley, "A Data-Driven Approximation of the Koopman Operator: Extending Dynamic Mode Decomposition," *Journal of Nonlinear Science*, vol. 25, no. 6, pp. 1307–1346, Dec. 2015.

[14] M. O. Williams, M. S. Hemati, S. T. Dawson, I. G. Kevrekidis, and C. W. Rowley, "Extending Data-Driven Koopman Analysis to Actuated Systems," *IFAC-PapersOnLine*, vol. 49, no. 18, pp. 704–709, 2016.

[15] Y. Meng, L. Li, X. Wang, W.-W. Huang, E. Q. Wu, and L. Zhu, "Online Koopman Operator-Based Feedforward Compensation Strategy for Fast Tool Servos With Robust High-Bandwidth Control," *IEEE Transactions on Industrial Electronics*, vol. 72, no. 3, pp. 2958–2967, Mar. 2025.

[16] D. Zhao, X. Yang, Y. Li, L. Xu, J. She, and S. Yan, "A Kalman-Koopman LQR Control Approach to Robotic Systems," *IEEE Transactions on Industrial Electronics*, vol. 71, no. 12, pp. 16 047–16 056, Dec. 2024.

[17] S. Yu, C. Shen, and T. Ersal, "Autonomous Driving using Linear Model Predictive Control with a Koopman Operator based Bilinear Vehicle Model," *IFAC-PapersOnLine*, vol. 55, no. 24, pp. 254–259, 2022.

[18] D. Bruder, X. Fu, and R. Vasudevan, "Advantages of Bilinear Koopman Realizations for the Modeling and Control of Systems With Unknown Dynamics," *IEEE Robotics and Automation Letters*, vol. 6, no. 3, pp. 4369–4376, July 2021.

[19] D. Goswami and D. A. Paley, "Global bilinearization and controllability of control-affine nonlinear systems: A Koopman spectral approach," in *2017 IEEE 56th Annual Conference on Decision and Control (CDC)*. Melbourne, Australia: IEEE, Dec. 2017, pp. 6107–6112.

[20] M. Wang, X. Lou, and B. Cui, "Deep bilinear Koopman realization for dynamics modeling and predictive control," *International Journal of Machine Learning and Cybernetics*, vol. 15, no. 8, pp. 3327–3352, Aug. 2024.

[21] D. Zhao, B. Li, F. Lu, J. She, and S. Yan, "Deep Bilinear Koopman Model Predictive Control for Nonlinear Dynamical Systems," *IEEE Transactions on Industrial Electronics*, vol. 71, no. 12, pp. 16 077–16 086, Dec. 2024.

[22] M. Abtahi, F. M. Araghi, N. Mojahed, and S. Nazari, "Deep Bilinear Koopman Model for Real-Time Vehicle Control in Frenet Frame," July 2025, arXiv:2507.12578 [eess].

[23] L. Shi, Z. Liu, and K. Karydis, "Koopman Operators for Modeling and Control of Soft Robotics," *Current Robotics Reports*, vol. 4, no. 2, pp. 23–31, July 2023.

[24] X. Zhang, M. Han, and X. Yin, "Reduced-order Koopman modeling and predictive control of nonlinear processes," *Computers & Chemical Engineering*, vol. 179, p. 108440, Nov. 2023.

[25] J. Wang, B. Xu, J. Lai, Y. Wang, C. Hu, H. Li, and A. Song, "An Improved Koopman-MPC Framework for Data-Driven Modeling and Control of Soft Actuators," *IEEE Robotics and Automation Letters*, vol. 8, no. 2, pp. 616–623, Feb. 2023.

[26] B. Lusch, J. N. Kutz, and S. L. Brunton, "Deep learning for universal linear embeddings of nonlinear dynamics," *Nature Communications*, vol. 9, no. 1, p. 4950, Nov. 2018.

[27] Y. Yang, Y. Jiang, W. Cao, C. Li, W. Jiang, H. Mo, X. Li, X. Xu, and X. Zhang, "Adaptive Deep Koopman Operators for Soft Robot Control: Application to Luban Lock Disassembly," *IEEE Transactions on Industrial Electronics*, pp. 1–12, 2026.

[28] L. Xiawen, M. Chetan, C. Shichao, W. Yajun, and D. L. R. Jaime, "Parameters determination of time-delayed embedding with application to Koopman operator-based model predictive frequency control," *CSEE Journal of Power and Energy Systems*, 2021.

[29] R. Moriyasu, S. Nojiri, A. Matsunaga, T. Nakamura, and T. Jimbo, "Diesel engine air path control based on neural approximation of nonlinear MPC," *Control Engineering Practice*, vol. 91, p. 104114, Oct. 2019.

[30] D. Zhao, C. Liu, R. Stobart, J. Deng, E. Winward, and G. Dong, "An Explicit Model Predictive Control Framework for Turbocharged Diesel Engines," *IEEE Transactions on Industrial Electronics*, vol. 61, no. 7, pp. 3540–3552, July 2014.

[31] H. Huang, X. Peng, W. Du, S. X. Ding, and W. Zhong, "Nitrogen Oxides Concentration Estimation of Diesel Engines Based on a Sparse Nonstationary Trigonometric Gaussian Process Regression With Maximizing the Composite Likelihood," *IEEE Transactions on Industrial Electronics*, vol. 70, no. 11, pp. 11 744–11 753, Nov. 2023.

[32] X. Wei and L. Del Re, "Gain Scheduled H_{∞} Control for Air Path Systems of Diesel Engines Using LPV Techniques," *IEEE Transactions on Control Systems Technology*, vol. 15, no. 3, pp. 406–415, May 2007.

[33] M. Iwadare, M. Ueno, and S. Adachi, "Multi-Variable Air-Path Management for a Clean Diesel Engine Using Model Predictive Control," *SAE International Journal of Engines*, vol. 02, no. 1, pp. 764–773, Apr. 2009.

[34] D. Gagliardi, T. Otsuka, and L. D. Re, "Direct C/GMRES Control of The Air Path of a Diesel Engine," *IFAC Proceedings Volumes*, vol. 47, no. 3, pp. 3000–3005, 2014.

[35] S. Yahagi, H. Seto, A. Yonezawa, and I. Kajiwara, "Sparse Identification and Nonlinear Model Predictive Control for Diesel Engine Air Path System," *International Journal of Control, Automation and Systems*, vol. 23, no. 2, pp. 620–629, Feb. 2025.

[36] S. H. Son, A. Narasingam, and J. S.-I. Kwon, "Handling plant-model mismatch in Koopman Lyapunov-based model predictive control via offset-free control framework," Oct. 2020, arXiv:2010.07239 [cs, eess].

[37] R. Haber and H. Unbehauen, "Structure identification of nonlinear dynamic systems—A survey on input/output approaches," *Automatica*, vol. 26, no. 4, pp. 651–677, July 1990.

[38] B. Schaible, Hong Xie, and Yung-Cheng Lee, "Fuzzy logic models for ranking process effects," *IEEE Transactions on Fuzzy Systems*, vol. 5, no. 4, pp. 545–556, Nov. 1997.

[39] Y. Xiao, X. Zhang, X. Xu, X. Liu, and J. Liu, "Deep Neural Networks With Koopman Operators for Modeling and Control of Autonomous Vehicles," *IEEE Transactions on Intelligent Vehicles*, vol. 8, no. 1, pp. 135–146, Jan. 2023.

[40] S. Kaneko, Y. Yamasaki, H. Ohmori, H. Mitsuo, I. Mizumoto, M. Ichiyanagi, A. Matsunaga, and T. Jimbo, *Model Based Control for Automotive engines*. CORONA, 2019.

[41] A. Yonezawa, H. Yonezawa, S. Yahagi, I. Kajiwara, S. Kijimoto, H. Taniuchi, and K. Murakami, "Sparse Identification of Nonlinear Dynamics With Library Optimization Mechanism: Recursive Long-Term Prediction Perspective," *IEEE Transactions on Cybernetics*, 2026.

[42] C. C. Zawacki and E. H. Abed, "Dynamic Mode Decomposition for Control Systems with Input Delays," *IFAC-PapersOnLine*, vol. 56, no. 3, pp. 97–102, 2023.

[43] H. Shi and M. Q.-H. Meng, "Deep Koopman Operator With Control for Nonlinear Systems," *IEEE Robotics and Automation Letters*, vol. 7, no. 3, pp. 7700–7707, July 2022.

[44] S. Ishizuka, I. Kajiwara, J. Sato, Y. Hanamura, and S. Hanawa, "Model-free adaptive control scheme for EGR/VNT control of a diesel engine using the simultaneous perturbation stochastic approximation," *Transactions of the Institute of Measurement and Control*, vol. 39, no. 1, pp. 114–128, Jan. 2017.